Materials Today Bio 5 (2020) 100032

Contents lists available at ScienceDirect

Materials Today Bio

journal homepage: www.journals.elsevier.com/materials-today-bio

Ceramics with the signature of wood: a mechanical insight

D. Bigoni [a,*], R. Cavuoto [a], D. Misseroni [a], M. Paggi [b], A. Ruffini [c], S. Sprio [c], A. Tampieri [c]

[a] DICAM, University of Trento, Via Mesiano 77, Trento, Italy
[b] IMT School for Advanced Studies Lucca, Italy
[c] CNR-ISTEC, Via Granarolo 64, Faenza, Italy

ARTICLE INFO

Keywords:
Hydroxyapatite
Mechanical properties
Strength
Fracture
Mechanical tests
Fractal porosity

ABSTRACT

In an attempt to mimic the outstanding mechanical properties of wood and bone, a 3D heterogeneous chemistry approach has been used in a biomorphic transformation process (in which sintering is avoided) to fabricate ceramics from rattan wood, preserving its hierarchical fibrous microstructure. The resulting material (called biomorphic apatite [BA] henceforth) possesses a highly bioactive composition and is characterised by a multiscale hierarchical pore structure, based on nanotwinned hydroxyapatite lamellae, which is shown to display a lacunar fractal nature. The mechanical properties of BA are found to be exceptional (when compared with usual porous hydroxyapatite and other ceramics obtained from wood through sintering) and unique as they occupy a zone in the Ashby map previously free from ceramics, but not far from wood and bone. Mechanical tests show the following: (i) the strength in tension may exceed that in compression, (ii) failure in compression involves complex exfoliation patterns, thus resulting in high toughness, (iii) unlike in sintered porous hydroxyapatite, fracture does not occur 'instantaneously,' but its growth may be observed, and it exhibits tortuous patterns that follow the original fibrillar structure of wood, thus yielding outstanding toughness, (iv) the anisotropy of the elastic stiffness and strength show unprecedented values when situations of stresses parallel and orthogonal to the main channels are compared. Despite being a ceramic material, BA displays a mechanical behavior similar on the one hand to the ligneous material from which it was produced (therefore behaving as a 'ceramic with the signature of wood') and on the other hand to the cortical/spongy osseous complex constituting the structure of compact bone.

1. Introduction

Wood and bone are natural materials displaying a similar and exceptionally performing mechanical behavior, which is rooted in their highly hierarchical and fibrous microstructure [1,2]. Therefore, mimicking of this microstructure to produce superior materials has been the objective of a massive research investment [3–26] (see Figs. 23 and 24).

In this vein, ceramics implementing a microstructure and nanostructure almost identical to wood can be easily believed to exhibit unprecedented mechanical performances and also to be ideal candidates for bone replacement. Following these ideas, biotemplating processes to fabricate 3D functional ceramics (such as apatites) from natural wood have been proposed, all terminating with sintering [5,7,8,10]. Recently, Tampieri et al. [27] developed a new procedure[1] to

* Corresponding author.
E-mail address: bigoni@ing.unitn.it (D. Bigoni).

[1] Even if the details of the process are reported in the studies by Tampieri et al [27–29], it may be important to mention that the maintenance of the complex architecture of wood was achieved through a chemical transformation process characterised by a very strict control of the reaction kinetics, which was obtained through the use of the equipment permitting the regulation and control of the temperature and pressure of reacting gases, thus establishing the more suitable thermodynamic conditions to reach a complete phase transformation in the whole solid [27]. Specifically, gas-solid reactions are strongly affected by various phenomena related to the adsorption of the gaseous reactant by the solid, the kinetics of nucleation and growth of the newly forming inorganic phase at the surface, and, most importantly, the penetration of the gaseous reactant in the inner regions of the structure so that only an effective control of all these processes yields the complete transformation of the template into the desired phase [30]. This control becomes more and more critical when large ceramic pieces are to be obtained because diffusive phenomena are predominant and regulate the rate of phase transformation. Hence, the strict control of the reaction kinetics is the key feature needed: (i) to activate the chemical reactions throughout the whole solid without inducing deformations and relevant structural defects, (ii) to limit the grain growth, thus maintaining the multiscale porosity, up to the nanosize, and (iii) to obtain highly reactive inorganic precursors, in turn facilitating subsequent transformation reactions [27]. This complex and challenging chemical process has been used to produce the samples of sufficiently relevant dimensions for our mechanical experiments (and also for bone replacement applications).

https://doi.org/10.1016/j.mtbio.2019.100032
Received 8 August 2019; Received in revised form 2 October 2019; Accepted 11 October 2019
Available online 24 October 2019

chemically transform rattan wood into a biomimetic hierarchically structured hydroxyapatite (HA). Unlike in previous approaches where the wood was infiltrated with HA slurries and finally sintered to eliminate the organic component and to consolidate the final ceramic [8,10], the new procedure can directly transform wood pieces into large HA scaffolds, preserving the original multiscale structure through a heterogeneous reaction under supercritical conditions directly in the 3D state, without adopting any sintering process. This is an important advantage because high-temperature treatments can represent a serious drawback for the scaffold bioactivity.[2] The resulting ceramic material (referred henceforth as 'biomorphic apatite' [BA]) not only maintains a highly bioactive composition and a multiscale pore hierarchy almost identical to those of the parent wood (thanks to a careful control of the reaction kinetics that prevents critical deformations at all scales and to the absence of sintering processes) but also shows a nanosize structure and unprecedented mechanical properties owing to great cohesion of the neo-formed nanocrystals [27]. BA represents a significant improvement in the development of 3D inorganic devices with a complex microstructure and multiscale details, which are relevant for smart functionality, which is still an open challenge owing to the ineffectiveness of the current ceramic fabrication processes.

The objective of the present study is the systematic investigation of the mechanical properties of BA, which are found to be similar to the mechanical properties of both wood and bone, so that BA becomes promising for bone regeneration, especially for load-bearing regions. A morphological investigation is reported, which shows that the porosity of BA displays a fractal nature of the lacunar type, a feature that may justify its excellent damage tolerance. In fact, the fractality of the porosity explains our experimental observation that the fracture is not abrupt and straight (as usual for ceramics) but evidences growth and tortuosity (as usual for bone). The results from an experimental campaign are presented, based on multiple mechanical tests: uniaxial compression (in both a standard configuration and *in situ* by scanning electron microscopy), three-point bending, ring tests, and ultrasound evaluations. It is shown that BA performs better than the standard HA [31,32] in several mechanical characteristics: elastic stiffness, strength, damage tolerance before failure, and related toughness. Moreover, unlike in HA and similar to wood and bone, BA is found to exhibit a strength in tension often superior to that in compression, to evidence a transversely isotropic behavior, which permits optimization of stiffness in the direction of loading, a feature particularly useful for bone replacement.

Our experiments allow the placement of BA in the Ashby charts, in terms of Young modulus vs strength or vs porosity, Fig. 1.

The Ashby charts reveal that BA occupies a virgin zone for ceramics and displays a similarity to the ligneous material from which it was 'born' and to several different bones, which evidences that the material is particularly suited for several biotechnologies.

It has to be finally mentioned that the results reported in the present study indicate that outstanding mechanical properties could be obtained for materials different from BA but obtained with a process similar to that used for BA, which can therefore be used as a guide for the fabrication of a new generation of inorganic materials with significant improvement in structural performance. This perspective is encouraged by previous results obtained with the chemical transformation of natural woods into various oxide (for instance, Al_2O_3, ZrO_2, TiO_2, and MnO) [33–37], and non-oxide (for instance, SiC, TiC, and ZrC) [38–42] ceramics, which are particularly relevant for structural applications.

[2] The drawback becomes particularly evident when the material's functionality is related to the presence of nanocrystalline, non-stoichiometric, or metastable phases, which can be easily degraded by high-energy processes. Moreover, sintering processes destroy the surface chemistry, reducing the biocompatibility of materials.

2. The lacunar fractal nature of porosity

Nanotwinned HA lamellae are a unique nanostructure characterizing BA [28] and form a complex multiscale porosity, where large pores (approximately 300 μm in diameter) are surrounded by medium-sized pores (up to 50 μm in diameter) and coexist with a distributed fine porosity (1 μm of diameter) (see the scanning electron microscopy image in Fig. 2). The fine porosity is alveolar and closed, whereas the large- and medium-sized porosity is two-dimensional so that longitudinal channels are present, closely resembling the structure of the wood from which the material was indeed originated.

To show that the porosity of BA possesses a lacunar fractal nature [43,44,51], images of microstructures captured by scanning electron microscopy at different magnifications (38 × , 100 × , and 250 × , in all cases using a variable pressure inside the scanning electron microscope (SEM) chamber in the 20 − 25MPa range) have been analyzed using an image recognition program *ad hoc* developed in MATLAB to filter the gray scale scanning electron microscopy images and transform them into binary data (depicted in yellow or blue in Fig. 3). This program allowed a fast computation of the apparent porosity of the material based on the ratio between the number of blue pixels and the total number of pixels. As usually occuring with real images, an intensity threshold of gray (a parameter ranging between 0 and 255) has to be introduced to filter the data and transform the gray scale image into black and white. Therefore, the curves in Fig. 4 show the evolution of the apparent porosity vs. the filter index, which is defined as the ratio between the aforementioned intensity threshold and the value 255, for the three scanning electron microscopy images acquired at different magnifications. The porosity is clearly resolution dependent, being an increasing function of the magnification. Such a resolution dependency reveals a lacunar fractal nature for BA. For a rigorous quantification, the box-counting method has been applied to compute the local fractal dimension of the lacunar domain D. For each box of lateral size r, the number N of boxes containing at least one black pixel is counted. This operation is repeated at varying r from 1 up to 512 lateral size divisions, with a geometric progression of 2. From the $N(r)$ relation, the local fractal dimension D of the porous material has been finally obtained by differentiating $\log N$ with respect to $\log r$, thus obtaining $D(r) = -\frac{\mathrm{d}(\log N)}{\mathrm{d}\log r}$. The results are presented in Fig. 5 where, for 500 computations equally sampled by varying the filter index between 0 and 0.3, the mean value of $D(r)$ (with their error bars, corresponding to $\pm s$, where s is the root mean square of the computed values) is plotted as a function of $\log r$. As expected, the local fractal dimension quantifying the effect of porosity is always less than 2, which corresponds to a Euclidean surface, over the whole range of r.

The fact that the porosity of BA has a lacunar fractality has a deep influence on the fracture propagation and trajectory, which (as shown later) is not abrupt and straight, but displays a growth with load in tortuous patterns which are unusual for ceramics and similar to bone [45,46].

3. Mechanical testings

Mechanical tests have been performed on 48 prismatic and 19 cylindrical samples and also on 17 hollow cylinders of BA and, for comparison, on 42 samples of two Engipore HAs [27].

Before testing, the chemical composition of the specimens has been investigated to assess the successful and complete transformation of rattan. This was verified through X-ray diffraction tests, one of which is presented inFig. 6, showing that the composition of HA is accompanied by relatively small quantities (less than 5%) of beta-tricalcium phosphate ($\beta - Ca_3(PO_4)_2$), represented by the black dots.

In the following section, a nomenclature borrowed from wood mechanics will be adopted for BA, namely, 'parallel or orthogonal to the grain' will denote alignment parallel or normal to the fibers (also denoting the direction of transverse isotropy) of the wood from which the

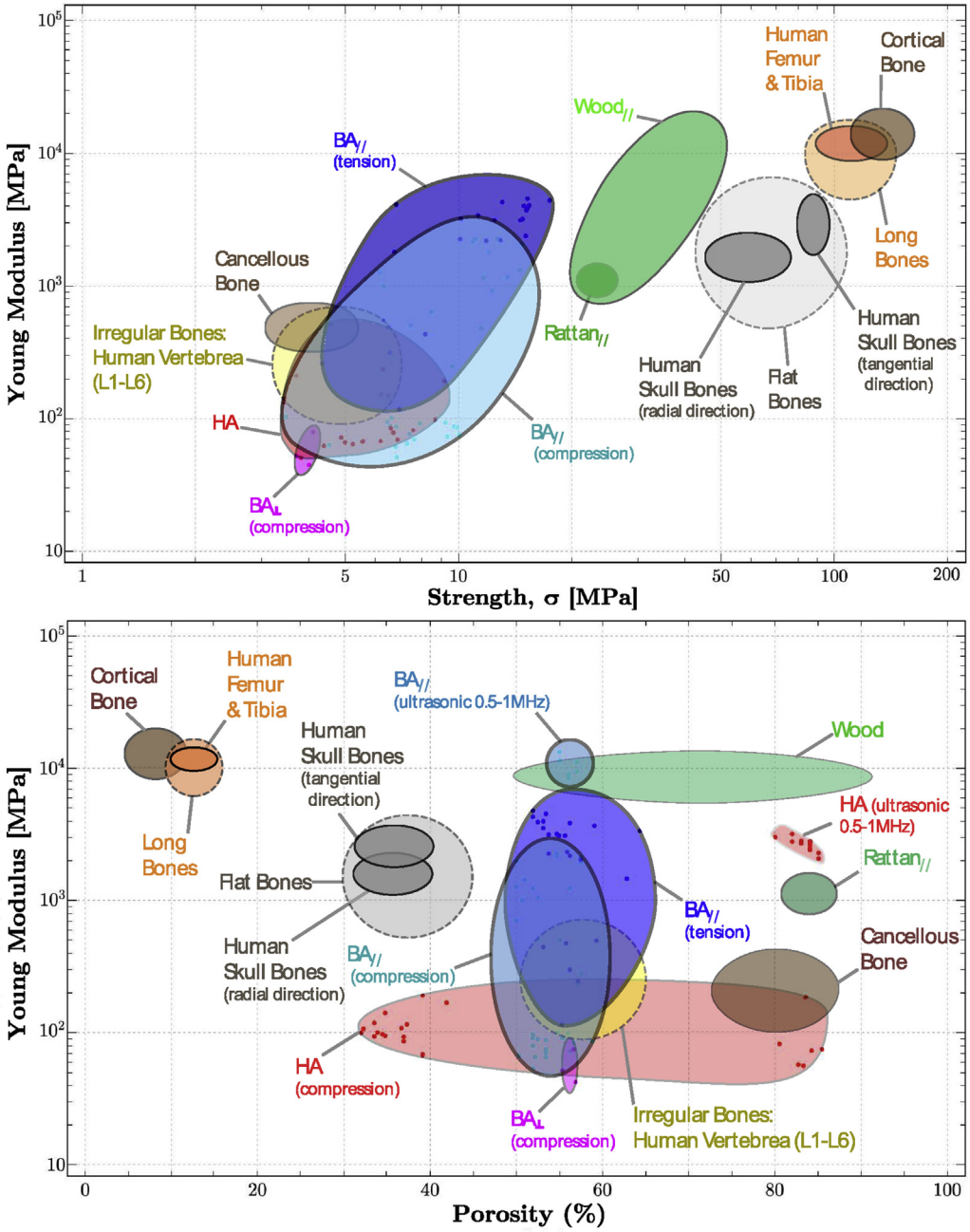

Fig. 1. Ashby charts reporting Young modulus vs strength (upper part) and vs porosity (lower part) for biomorphic apatite, loaded parallel (BA/ /) and perpendicular (BA⊥) to the microtubule structure ('grain' in the following), for rattan wood (from which BA was obtained), and for bones. BA, biomorphic apatite; HA, hydroxyapatite.

ceramic was made.

The results of (i) uniaxial compression tests, (ii) three-point bending, and (iii) ring tests are summarized respectively for the two materials in Tables 1 and 2, where mean values and standard deviations are reported. Note that the first two tests have been performed following the standards [47,48].

Values of compression σ_c, tension strengths σ_t, and elastic modulus E (index 'c' in compression; index 'f' in flexure), are summarized in Tables 1 and 2

Different stocks of ceramics (four for BA and two for HA) have been investigated; for BA, these will be denoted by a number (#1, #2, #3, #4), whereas for HA, it will be denoted by HA1 and HA2. The samples have been *ad hoc* produced in different shapes to allow the execution of multiple mechanical tests. The mass density was varying for different stocks, so that the results presented in all tables (except Tables 8 and 10) and in all figures (except Fig. 24) have been reported (with a linear proportion) to the same value of the mass density, $\rho_0 = 1.47\ \mathrm{g/cm^3}$, assumed as the reference (as it was the most representative value for BA).

The possibility of using ultrasonic tests has also been analyzed (on 6 samples taken from stocks #1 and #2) to investigate the mechanical properties of BA on a scale much smaller than that explored through the other mechanical tests and typical of the cells forming bone tissues (osteoblasts).

An additional series of compressive tests were performed on prismatic samples by scanning electron microscopy, with different purposes: (i) to assess the role of friction between the steel platens and BA prismatic specimens, (ii) to document crack pattern evolution and sample exfoliation under uniaxial compression, and (iii) to evaluate the effect of the

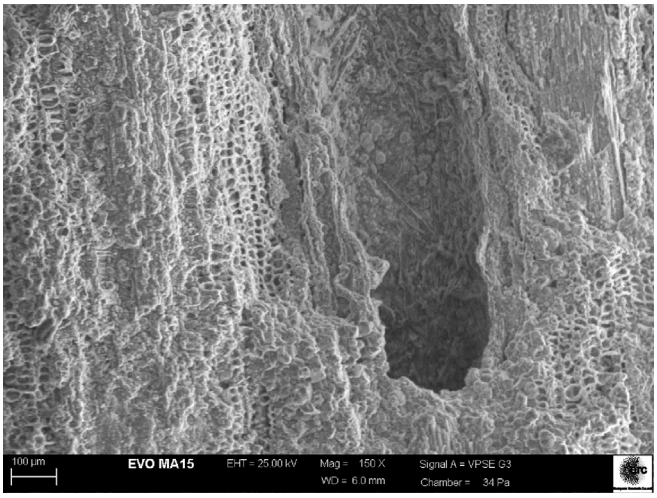

Fig. 2. An scanning electron microscopy image of the microstructure of biomorphic apatite showing long open channels surrounded by finer alveolar closed pores.

eccentricity in the axial load, which can be caused in real applications by local imperfections in the specimen geometry and by inhomogenity of the material's microstructure. In a first experiment, the BA specimen has been tested under uniaxial compression with steel platens in direct contact with the BA specimen, which leads to a contact problem with high friction. In a second experiment, a high-density polyethylene layer has been interposed at the interface between the specimen and steel platen to reduce friction, whereas the opposite interface has been left with friction. Finally, a third experimental setup has been designed (through the interposition of paper board layers) to induce eccentric compression at low friction with the steel platens. Further evidence is provided in videos filmed during different tests (see Support electronic material).

Mechanical tests were conducted at the Instability Lab (University of Trento) using a Midi 10 and a Beta 100 electromechanical testing machines (Messphysik Materials Testing) used in different configurations for uniaxial compression tests, three-point bending, and ring tests (on hollow cylinders), which are detailed in this section. Additional in situ compression tests were conducted with the tensile/compression stage DEBEN 5000S from GATAN, which is placed within the SEM EVO MA15

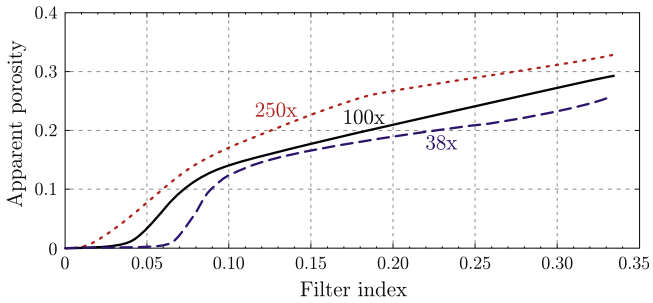

Fig. 4. Increase of apparent porosity for BA with the filter index at different magnification scales, showing the lacunar fractal nature of BA. BA, biomorphic apatite.

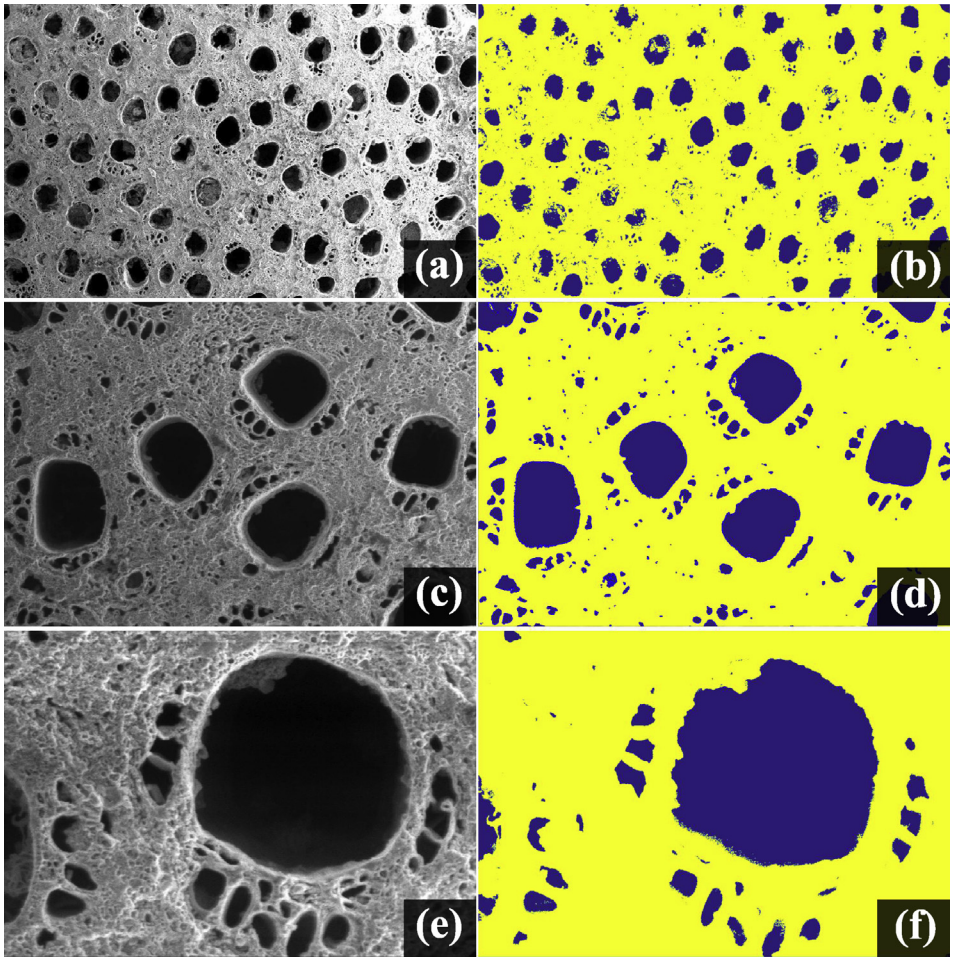

Fig. 3. Scanning electron microscopy images of cross sections of biomorphic apatite (BA) and the corresponding apparent porosity identified on the basis of the application of an ad hoc image analysis software with a filter index of 0.2. In particular, (a) 38× scanning electron microscopy image of BA; (b) at 38 × , the porosity is detected to be 14.6%; (c) 100× scanning electron microscopy image of BA; (d) at 100 × , the porosity is detected to be 19.0%; (e) 250× scanning electron microscopy image of BA; (f) at 250 × , the porosity is detected to be 27.0%. The image correlation software shows that porosity is increasing with the magnification, and this reveals the lacunar fractality of the cross section domain. BA, biomorphic apatite.

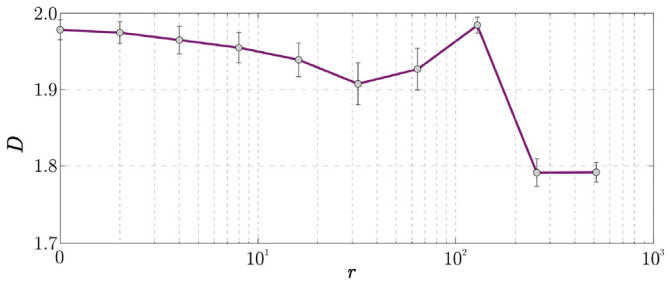

Fig. 5. Local fractal dimension D (which quantifies the porosity) as a function of r (the lateral side division of the image in the box-counting algorithm).

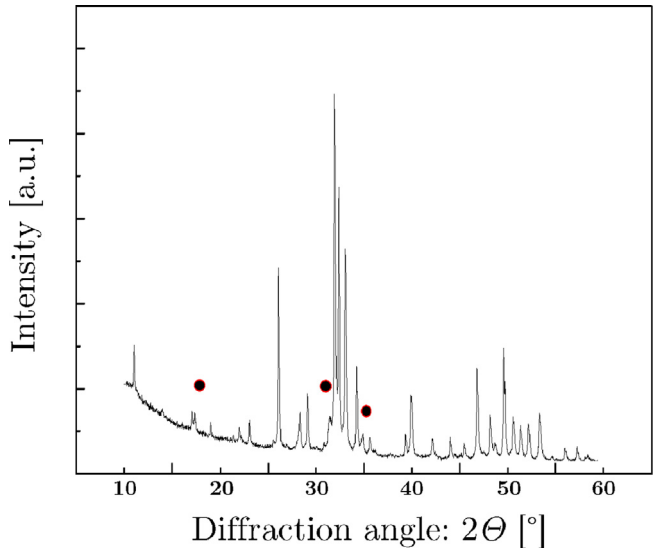

Fig. 6. XRD (x-ray diffraction) pattern of one sample of bioapatite used for mechanical tests, where the dots point to reflections addressing the β-TCP phase. All the unmarked peaks point to the HA phase. HA, hydroxyapatite; β-TCP, beta-tricalcium phosphate.

from Zeiss, both available in the MUSAM-Lab (the experimental laboratory of the Multi-scale Analysis of Materials Research Unit at the IMT School for Advanced Studies Lucca).

3.1. Uniaxial compression test

BA and HA prismatic and cylindrical samples and BA tubular samples have been tested under uniaxial compression. While HA is isotropic and does not show any orientation characteristic, BA is strongly anisotropic (owing to its fibrous nature inherited from wood) so that compression has been applied both parallel and orthogonal to the fibers. (Both tests have been performed only on prismatic samples, whereas cylindrical samples have been tested only parallelly to the fibers.) The sample, in direct contact with two circular steel platens (40-mm diameter and 5-mm thick), is compressed by imposing displacements to the upper platen. Fig. 7 reports a sequence of photos taken during a typical uniaxial compression test on a BA cylindrical sample and related to the corresponding stress/strain curve (reported in the following section). For comparison, in Fig. 8, a uniaxial compression test on standard HA is reported, which abruptly fails as soon as a splitting crack (visible in the photo) is enucleated.

The photos show a progressive failure with continuing exfoliation for the BA sample compressed parallel to the grain, in sharp contrast with the typically brittle failure displayed by HA (Fig. 8 and the study by Libonati et al [49]). The exfoliation failure pattern is similar to that documented by Gei et al. [50] for silicon nitride at high temperature but is now much more pronounced and yields a much more evident softening in the stress/strain curve (see Fig. 9) where a result for BA is reported (on the left) and contrasted with an analogous result for HA (on the right). Note that the stress/strain curves have been both reported to the reference density of 1.47 g/cm^3.

Note that BA evidences a higher peak strength than HA, both occurring practically at the same strain level, but while HA is abruptly crushed at that strain, exfoliation takes place for BA, which continues to carry load and attains a final strain of more than 35%, thus displaying a great toughness for a ceramic.

Further results from compression tests parallel to the grain are reported in Table 3, for four different stocks of BA, each one characterized by different geometries and dimensions. The results are contrasted with the analogous for the two standard HAs, also reported in Table 3.

It can be observed in Table 3 that the fibrous microstructure of BA implies that during compression parallel to the grain, the sample is not in perfect contact with the loading platens, an effect which produces a pronounced scattering of experimental results and is detrimental to the measured strength. This effect is much less pronounced for HA samples, where parallelism and planarity of the surfaces can be better obtained than for BA.

Prismatic samples from stock BA #4 have been compressed orthogonally to the grain (i.e., normally to the weak plane), with the same experimental configuration used for other compression tests. A sequence of photos during this compression is reported in Fig. 10, showing the progressive formation of a set of inclined fractures, something that would be hardly visible for standard HA.

In the direction orthogonal to the grain, BA is weaker than HA, as a consequence of the highly oriented microstructure of BA, providing strong transverse isotropy in strength and also in elastic stiffness. This can be observed from the stress/strain curve reported in Fig. 11, typical

Table 1
Summary of the mechanical properties of biomorphic apatite (BA), obtained from uniaxial compression, three-point bending, and compression ring tests on samples of different geometry (prismatic, cylindrical, and tubular). All the mechanical properties are expressed in terms of their average ± standard deviation: σ_c, strength in compression; σ_t, strength in tension; E_c, Young modulus in compression; E_f, Young modulus in flexure; index, ' ∥ ' and ' ⊥ ' stand for parallel and orthogonal to the grains, respectively. Finally, ρ/ρ_0 is the ratio between the density and the reference density of 1.47 g/cm^3 to which all mechanical values have been reported.

	Uniaxial compression (∥)			Uniaxial compression (⊥)			3-point bending (∥)			Ring test (⊥)	3-point bending (⊥)	
	#1,2. #3. #4.			#4.			#1,2. #4.			#3.	#4.	
Sample Set	$\sigma_{c\parallel}$ [MPa]	$E_{c\parallel}$ [MPa]	ρ/ρ_0 [–]	$\sigma_{c\perp}$ [MPa]	$E_{c\perp}$ [MPa]	ρ/ρ_0 [–]	$\sigma_{t\parallel}$ [MPa]	$E_{f\parallel}$ [MPa]	ρ/ρ_0 [–]	$\sigma_{t\perp}$ [MPa]	$E_{f\perp}$ [MPa]	ρ/ρ_0 [–]
# 1	6.5 ± 3.0	216 ± 99	0.95	–	–	–	8.7 ± 3.1	3426 ± 1448	0.83	–	–	–
# 2	7.7 ± 1.6	79 ± 13	1.01	–	–	–	13.8 ± 2.5	3342 ± 884	1.00	–	–	–
# 3	10.8 ± 2.9	1011 ± 448	1.06	–	–	–	–	–	–	6.0 ± 0.94	2851 ± 1152	1.1
# 4	12.3 ± 1.6	2201 ± 147	0.96	3.9 ± 0.1	59 ± 18	0.96	6.4 ± 1.5	359 ± 157	0.97	1.1 ± 0.6	8.0 ± 1.8	1.00

Table 2
Summary of the mechanical properties of commercial hydroxyapatite (HA), obtained from uniaxial compression and three-point bending tests on prismatic samples.

Sample set	Uniaxial compression			Three-point bending		
	σ_c [MPa]	E_c [MPa]	ρ/ρ_0 [−]	σ_t [MPa]	E_f [MPa]	ρ/ρ_0 [−]
HA 1	6.2 ± 2.5	239 ± 131	0.36	3.5 ± 0.6	3686 ± 1087	0.36
HA 2	5.6 ± 1.6	79 ± 23	1.41	5.7 ± 0.8	5235 ± 886	1.27

HA, hydroxyapatite.
All the mechanical properties are expressed in terms of their average ± standard deviation: σ_c, strength in compression; σ_t, strength in tension; E_c, Young modulus in compression; E_f, Young modulus in flexure. ρ/ρ_0 is the ratio between the density and the reference density of 1.47 g/cm^3, to which all mechanical values have been reported.

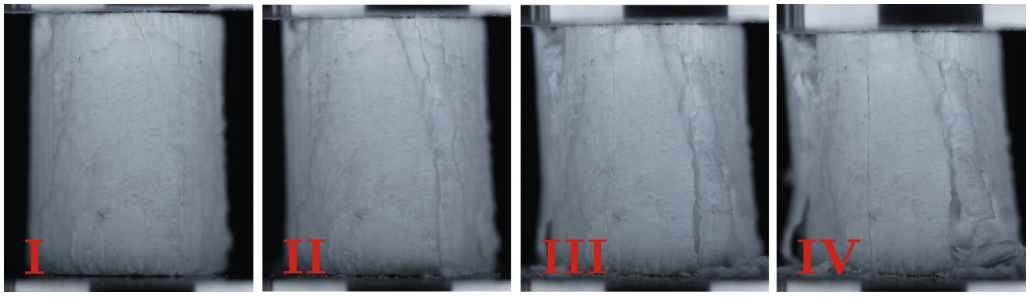

Fig. 7. A sequence of photos taken during a uniaxial compression test of a cylindrical sample of BA. The instances when the photos have been taken are marked on the stress/strain curve (Fig. 9 on the left) reported in the following. Note the progressive exfoliation of the sample, strongly enhancing toughness and related to the peaks in the stress/strain diagram. BA, biomorphic apatite.

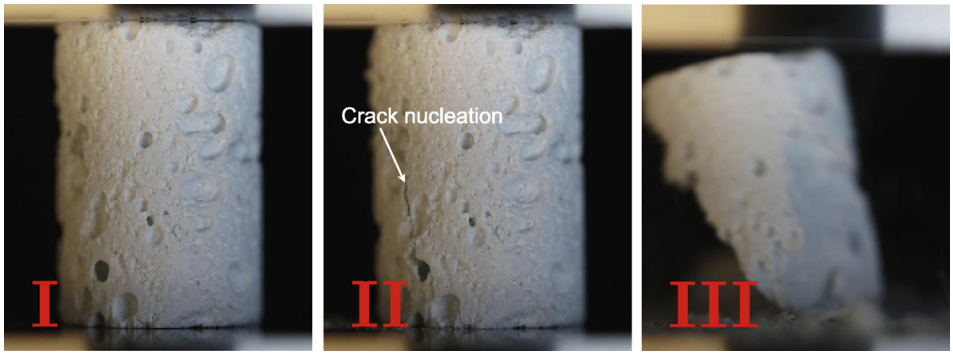

Fig. 8. A sequence of photos taken during a uniaxial compression test of hydroxyapatite samples. The instances when the photos have been taken are marked on the stress/strain curve (Fig. 9 on the right) reported in the following. Note the abrupt failure of the specimen immediately after the appearance of a splitting crack.

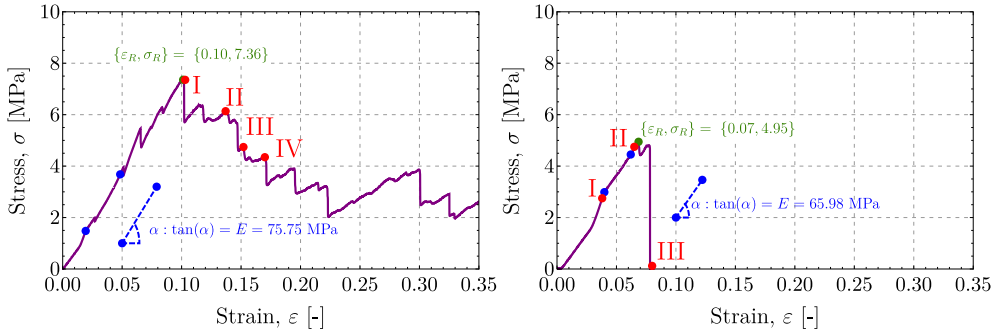

Fig. 9. Stress/strain behavior of a BA sample (#1, on the left) and of a HA sample (#1, on the right) subject to uniaxial compression, parallel to the grain for BA. The green spot identifies the peak strength, and a straight line drawn through the two indicated blue spots was used to evaluate the Young modulus $E = \tan\alpha$. The superior toughness of BA is evidenced by the slow load fall, contrasting with the sharp jump to zero displayed by HA.

for compression orthogonal to the grain of BA prismatic samples. However, although strength and stiffness orthogonal to the grain are noticeably inferior to those measured parallel to the grain, BA still retains an excellent toughness.

Compression orthogonal to the BA fibers was performed on prismatic samples only. In Table 4, the geometric properties of such samples are reported, along with the mechanical results of the tests.

Table 3
Mechanical characteristics from uniaxial compression tests on different stocks of BA and HA (compression parallel to the grain for BA).

Sample set	Geometrical properties				Uniaxial compression test		
	ϕ [mm]	H [mm]	A [mm^2]	ρ [g/cm^3]	$\sigma_{c\parallel}$ [MPa]	$E_{c\parallel}$ [MPa]	ρ/ρ_0 [−]
# 1	14.30	19.89	160.62	1.39	6.5 ± 3.0	216 ± 99	0.95
# 2	15.21	19.83	181.62	1.49	7.7 ± 1.6	79 ± 13	1.01
# 3	29.35	31.13	511.29	1.56	10.8 ± 2.9	1011 ± 448	1.06
# 4	19.47	31.22	213.27	1.44	12.3 ± 3.2	2201 ± 147	0.96
HA 1	10.07	14.29	79.59	0.54	6.2 ± 2.5	239 ± 131	0.36
HA 2	10.03	14.75	79.05	2.07	5.6 ± 1.6	79 ± 23	1.41

HA, hydroxyapatite; BA, biomorphic apatite.
On the left, the averages of the geometrical properties of each stock are shown: ϕ is the main dimension of the samples' base (which corresponds to the outer diameter of samples #1, #2, #3 and to a side of the prismatic sample #4); H is the height; A is the average cross-sectional area, and ρ is the average density. On the right, the following average properties (± standard deviation) are reported (from left to right): compressive strength and Young modulus. Finally, ρ/ρ_0 is the ratio between the density and the reference density of 1.47 g/cm^3 to which all mechanical values have been reported.

3.2. Three-point bending tests

Three-point bending tests have been carried out to evaluate the tensile stiffness and strength of BA and for comparison of HA. The tests have been performed by imposing the vertical displacements of a steel tip placed at the centerline of a prismatic sample, supported by two cylindrical elements placed at a distance L. The values of the stress σ, strain ε, and elastic Young modulus in tension E_f are determined, respectively, from the value of the applied load P and deflection at centerline v and from a difference between two selected values of the load ΔP (measured during elastic response of the sample), together with the corresponding difference between midspan deflections Δv. The specimen is treated as a linear elastic beam [52] as follows:

$$\sigma = P\frac{L\,h}{8\,I}, \quad \varepsilon = v\frac{6\,h}{L^2}, \quad E_f = \frac{\Delta P}{\Delta v}\frac{L^3}{48\,I}, \tag{1}$$

where I is the moment of inertia of the cross section, L is the distance between the supports, and h is the height of the cross section.

The three-point bending test with tension parallel to the grain was carried out on BA and HA samples for comparison to evaluate the tensile elastic stiffness and strength in the direction parallel to the grain. A sequence of photos taken during a three-point bending test on BA is reported in Fig. 12, showing a feature rarely visible in a ceramic sample,

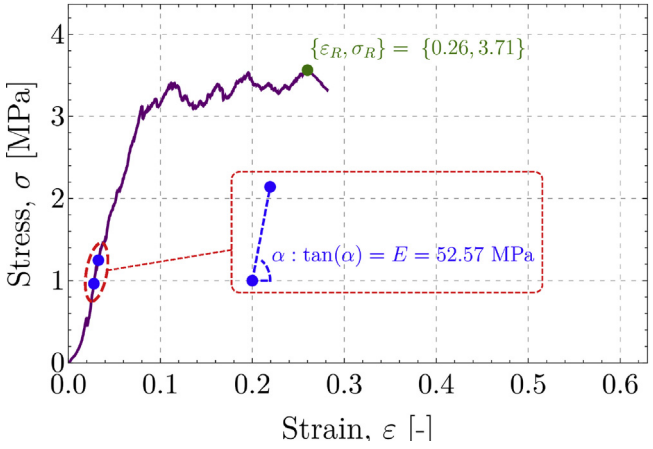

Fig. 11. Stress/strain behavior of a BA sample compressed parallel to the grain. The green spot identifies the peak strength, and a straight line drawn through the two indicated blue spots was used to evaluate the Young modulus $E = \tan\alpha$. BA, biomorphic apatite.

Fig. 10. A sequence of photos showing progressive failure during uniaxial compression orthogonal to the grain of a BA prismatic sample (from set #4, geometrical and mechanical properties reported in Table 4). BA, biomorphic apatite.

Table 4
Mechanical characteristics from uniaxial compression tests orthogonal to the grain.

Sample set	Geometrical properties					Uniaxial compression test		
	B [mm]	H [mm]	S [mm]	A [mm^2]	ρ [g/cm^3]	$\sigma_{c\perp}$ [MPa]	$E_{c\perp}$ [MPa]	ρ/ρ_0 [−]
# 4	40.51	10.21	19.72	799.01	1.41	3.9 ± 0.1	59 ± 18	0.96

All samples are prismatic, with the following average dimensions: *B* width; *H* height; *S* depth; *A* cross-sectional area; and ρ density. On the right, the following average properties (± standard deviation) are reported (from left to right): compressive strength and Young modulus. Finally, ρ/ρ_0 is the ratio between the density and the reference density of 1.47 g/cm^3 to which all mechanical values have been reported.

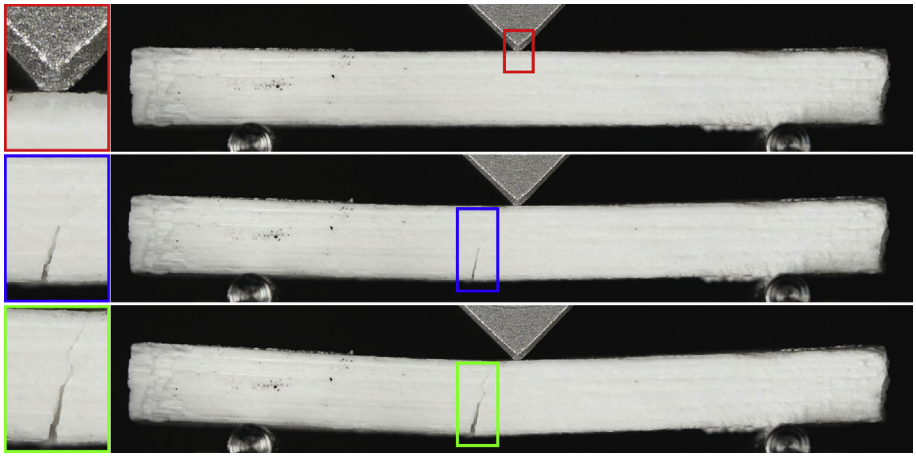

Fig. 12. A sequence of photos taken during a three-point bending test on the prismatic sample of biomorphic apatite (BA set # 1), tested in the direction parallel to the grain. The growth of a tensile fracture is clearly documented. (See the insets marked blue and green; the inset marked red shows a detail of the loading blade.) BA, biomorphic apatite.

namely, the growth of a tensile crack, something which cannot be observed in a HA sample and again demonstrating the superior damage tolerance of BA.

A typical stress/strain curve obtained from a three-point bending test is shown in Fig. 13, on the left for BA (with tension parallel to the grain) and on the right for HA.

Further results on mechanical properties measured in bending (with tension parallel to the grain for BA) for different stocks are presented (in terms of average stress and stiffness) in Table 5.

Table 5 shows that the mechanical properties, in particular the elastic Young modulus of BA, are noticeably different from stock to stock. This effect can be related to the different aspect ratio (H/L) of the specimens as this parameter influences the failure mechanism of the sample. In fact, stock #4 is characterized by an aspect ratio 2.5 times higher than that for the other stocks (BA #1, #2). Therefore, a shear mechanism of failure prevails, leading to an underevaluation of the Young modulus.

The three-point bending test with tension orthogonal to the grain was carried out on BA samples to evaluate the tensile stiffness and strength in that direction. A sequence of photos taken during a test is reported in Fig. 14, showing once more the growth of a tensile crack, again something rarely visible in ceramics and documenting the great toughness of BA.

A typical stress/strain curve obtained from a three-point bending test for tensile stress orthogonal to the grain is shown in Fig. 15.

Further results on mechanical properties measured in bending with tensile stress orthogonal to the grain are presented (in terms of average stress and stiffness) in Table 6.

Table 6 shows that the mechanical properties of BA, evaluated orthogonally to the grain, in particular the elastic Young modulus, are significantly lower than the same properties evaluated in the direction parallel to the grain. The fact that the measured values are much smaller than those referred to tests parallel to the grain (and also are smaller than the values obtained with the ring test presented in the next section) is related to the dimensions of the samples, which are too thick to be represented as beams, so that the failure shown in Fig. 14 is more related to the shear force applied by one support than to flexure.

3.3. Ring tests

The ring test is performed on tubular samples that are compressed along the diametral direction until failure occurs. This setup is similar to the so-called 'Brazilian test,' except that the samples for the latter test are solid cylinders. Both tests are used to investigate the tensile mechanical properties of brittle materials. Consistently, the ring test has been thoroughly used for rocks as these materials are brittle (as ceramics) so that the tensile properties can be inferred from a compressive experimental setup.

Many works [53–56] have shown that the tensile strength of a linear elastic, perfectly brittle material evaluated in the ring test is a function of the ratio between the internal and external radii $\bar{r}$. Nonetheless, for values of $\bar{r}$ more than 0.3, Hudson [57] proved that the evaluated tensile strength tends to become a constant quantity, in other words, the strength results unaffected by such ratio. Furthermore, Srinath and Acharya [58] demonstrated that the beam theory [52] is effective in the evaluation of the tensile strength of ring specimen for values of $\bar{r}$ ranging between 0.6 and 1, in other words, when the ring thickness is very small. Because in our study $\bar{r} = 0.512 \pm 0.009$, the stress/strain relation σ/ε has been obtained by the following equation:

$$\sigma = P\,\frac{h\,R}{2\pi\,I}, \quad \varepsilon = v\,\frac{8\,h}{(\pi^2-8)R^2}, \tag{2}$$

where v is the vertical displacement of the steel plate applying the force P to the specimen, R is the average between external and internal radii, h is the thickness of the cylinder wall, and I is its moment of inertia.

It should be noted that the ring tests are loading the sample in the

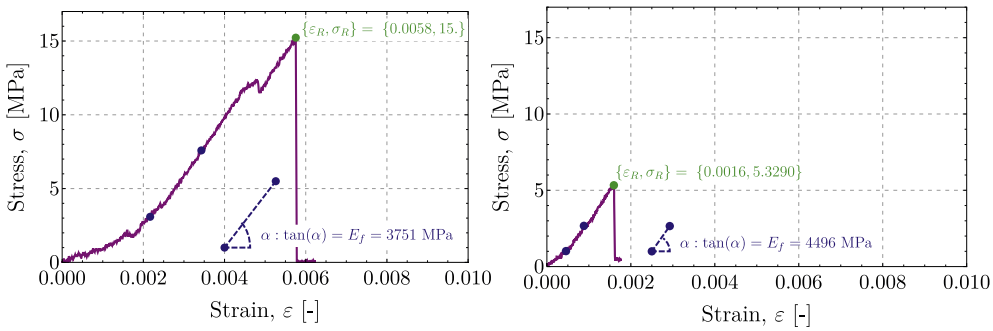

Fig. 13. Tensile stress/strain behavior of BA (set #1, on the left) and of HA (set # 2, on the right) from a three-point bending test, parallel to the grain for BA. The green spot identifies the peak strength, and a straight line drawn through the two indicated blue spots was used to evaluate the Young modulus $E = \tan\alpha$. The superior toughness of BA is highlighted by the failure strain much higher than in the HA sample. BA, biomorphic apatite; HA, hydroxyapatite.

Table 5
Mechanical characteristics from three-point bending tests on the different stocks of BA (with tension parallel to the grain) and HA.

Sample set	Geometrical properties				Three-point bending parallel to the grain		
	B [mm]	H [mm]	L [mm]	P [g/cm^3]	$\sigma_{t\parallel}$ [MPa]	$E_{f\parallel}$ [MPa]	ρ/ρ_0 [−]
# 1	11.04	5.72	37.33	1.22	8.7 ± 3.1	3426 ± 1448	0.83
# 2	9.94	5.21	35.00	1.47	13.8 ± 2.5	3341 ± 884	1.00
# 4	19.49	10.10	26.00	1.42	6.4 ± 1.5	359 ± 157	0.97
HA 1	10.03	5.11	40.00	0.53	3.5 ± 0.6	3686 ± 1087	0.36
HA 2	10.16	5.00	35.00	1.81	5.7 ± 0.8	5235 ± 886	1.27

BA, biomorphic apatite; HA, hydroxyapatite.
All the samples are prismatic, with the following average dimensions: B depth; H height; L length; and ρ density. On the right, the following average properties (± standard deviation) are reported (from left to right): tensile strength and Young modulus. Finally, ρ/ρ_0 is the ratio between the density and the reference density of 1.47 g/cm^3 to which all mechanical values have been reported.

'weak' direction, orthogonal to the grain, so that these tests are particularly suited to reveal the less stiff and less resistant behavior of the material.

A sequence of photos taken during the testing of BA is reported in Fig. 16, showing initially the growth of two vertical tensile cracks and later of two horizontal tensile cracks, terminating the load-carrying capacity of the specimen. This growth of a tensile fracture, as already observed for three-point bending tests, is unusual for ceramic materials, which usually display a sudden failure.

A typical stress/strain curve obtained from a ring test (tensile stresses orthogonal to the grain) is shown in Fig. 17.

Further results of the mechanical tests are shown in Table 7, together with the geometrical properties of the samples.

The results in Table 7 report good values of strength for BA subjected to tension orthogonal to the grain, values better than those obtained from three-point bending. Fig. 17 displays an interesting feature, namely, a double peak in the stress/strain curve, which shows that the maximum tensile strength is achieved twice: first time at the first vertical cracking and a second time at the formation of the horizontal crack. Before cracking, the sample is a ring loaded with two opposite concentrated forces, but after the first crack has formed, the static scheme changes to an arch loaded with two opposite forces acting on its springer points. This new configuration reminds that of the half ring test [59], where the tensile strength of the specimen is obtained by using the Beer's formulation of a prismatic circular arch.

3.4. Ultrasonic tests

The multiscale structure of BA requires a mechanical characterization both in the macroscale, for load-bearing applications, and nanoscale, for the interaction of BA with bone cells. Therefore, in addition to the mechanical tests performed at the scale of the sample, ultrasonic measurements were taken at high wavelength in an attempt to characterize the elastic properties of the material at a microscale. P-waves were used (generated and recorded using a pressure wave transducer, Olympus A102S, frequency 1 and 0.5 MHz, connected to an ultrasonic square wave

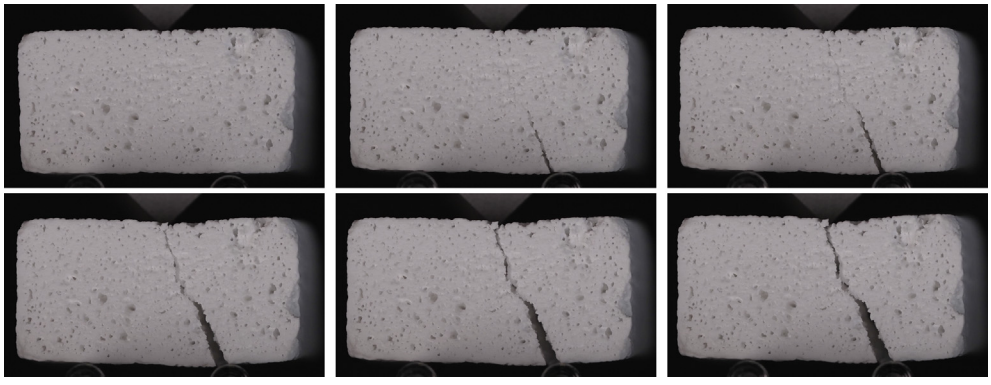

Fig. 14. A sequence of photos taken during a three-point bending test on biomorphic apatite prismatic samples (set #4) tested in the direction orthogonal to the grain. Note the growth of a tensile fracture.

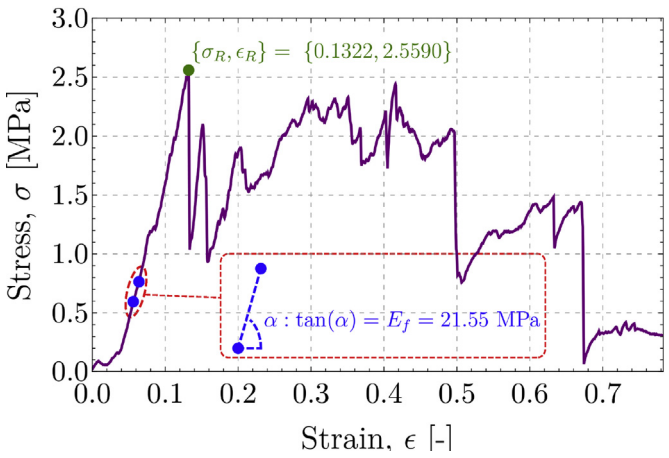

Fig. 15. Tensile stress/strain behavior of BA (set #4) from a three-point bending test, with tensile stress parallel to the grain. The green spot identifies the peak strength, and a straight line drawn through the two indicated blue spots was used to evaluate the Young modulus $E = \tan\alpha$. The high toughness of BA is highlighted by the slow load fall. BA, biomorphic apatite.

Table 6
Mechanical characteristics from three-point bending tests with tension orthogonal to the grain.

Sample set	Geometrical properties				Three-point bending orthogonal to the grain		
	B [mm]	H [mm]	L [mm]	ρ [g/cm^3]	$\sigma_{t\perp}$ [MPa]	$E_{f\perp}$ [MPa]	ρ/ρ_0 [−]
# 4	37.00	10.13	12.07	1.44	1.9 ± 1.2	11 ± 7	0.98

All the samples are prismatic, with the following average dimensions: B depth; H height; L length; ρ density. On the right, the following average properties (± standard deviation) are reported (from left to right): tensile strength and Young modulus. Finally, ρ/ρ_0 is the ratio between the density and the reference density of 1.47 g/cm^3 to which all mechanical values have been reported.

pulser/receiver unit, Olympus 5077 PR, combined with a NI PCI-5152 Digitizer/Oscilloscope). The tests were performed by measuring the time t_v needed for P-waves to travel along the height H of the sample and reach a sensor so that the velocity of the wave is given by $v_p = H/t_v$, which, for an isotropic elastic material, is linked to the Lamé constants through

$$v_p = \sqrt{\frac{\lambda + 2\mu}{\rho}}, \tag{3}$$

so that the elastic modulus E may be evaluated, once the Poisson's ratio ν is known, from the following equation.

$$E = \frac{(\lambda + 2\mu)(1+\nu)(1-2\nu)}{1-\nu}. \tag{4}$$

The result of two typical ultrasonic tests on BA (right) and HA (left) is shown in Fig. 18 at two different frequencies (0.5 and 1.0 MHz), in terms of signal amplitude ('Amp') versus time.

Mechanical properties derived from ultrasonic tests (parallel to the grain) are reported in Table 8, in terms of mean values of uniaxial strain elastic modulus $\lambda + 2\mu$ and Young modulus E, the latter evaluated for two extreme values of Poisson's ratio ν. Note that the data collected in Table 8 have not been reported to the reference density because in an ultrasonic test, the measurements are believed to be referred to the skeleton material.

It is worth mentioning that knowing the frequencies of the applied P-wave and its speed allows checking the wavelength of the applied exciting pulse as follows:

$$\lambda_p = \frac{v_p}{f_p} \approx \frac{2500 \text{ m/s}}{10^6 \text{ Hz}} = 2.5 \text{ mm}, \tag{5}$$

Which is higher than the typical dimensions of osteoblasts (on the order of 20 μm), so that the elasticity detected using the ultrasound tests is not believed to be representative of the scale of a single cell, but may still be acceptable to characterize the biological response of the material because these osteoblasts tend to interact with bone in large groups rather than individually.

3.5. *In situ* mechanical tests and further analysis of crack patterns

A series of compression tests were performed using a micro-mechanical compressive stage placed inside a SEM (Zeiss EVO MA15 equipped with the DEBEN5000S tensile/compressive stage) with the purpose of analyzing the effects of boundary conditions on the samples and the fracture paths typical of BA.

Compression is applied under displacement control with a gearbox speed of 0.1 mm/min to achieve quasi-static conditions. The equipment has a 10-mm linear extensometer for position readout, with 300-nm resolution. The combined use of the stage and the SEM allows inspection of the evolution of the crack pattern and the role of the material microstructure during the application of axial displacement. Three BA prismatic specimens, whose geometrical data are collected in Table 9, were tested under different boundary conditions to assess the sensitivity of the material response and of the fracture pattern upon variations from a reference testing configuration characterized by uniaxial compression with steel platens in direct contact with the specimen (where friction is present at the interface between steel and BA).

In the first test, the BA specimen is inserted between the steel platens without introducing measures to reduce friction and is loaded under uniaxial compression. The overall stress/strain mechanical response is represented by the red curve in Fig. 19, labeled as 'high friction.' The progress of the crack pattern inspected by scanning electron microscopy imaging shows the appearance of cracks predominantly aligned with the axial direction, parallel to the grain (Fig. 20). The stress/strain curve shows a peak stress of 9 MPa, corresponding to first cracking, followed by a plateau and a progressive hardening continuing up to $\sigma \approx 10 - 11$ MPa and a significant toughness at failure so that the failure strain is $\varepsilon \approx 0.05$. The failure strength observed from the test is consistent with that obtained on similar specimens using the Messphysik Materials Testing, reporting $\sigma \approx 12.3$ MPa (Table 1, first column, fourth row).

In the second test, a high-density polyethylene layer (visible in Fig. 21) is inserted at the contact between one of the BA bases and the steel platen so that friction is reduced on one base but not on the opposite base. The overall stress/strain curve is shown by the blue curve in Fig. 19, labeled as 'low friction.' The perturbed boundary conditions have not significantly modified the values of the failure strength and of the corresponding deformation, when compared with the 'high friction' case. However, the crack pattern leading to failure was found substantially different, with the appearance of a major exfoliating crack perpendicular to the grain direction and clearly visible on the specimen surface (Fig. 21). Inspection of the specimen after failure also showed the existence of many cracks aligned parallel to the grain direction, again as observed in the 'high friction' case (see Fig. 22).

In the third test, the BA specimen was inserted with paperboard layers at both its bases to reduce friction on both sides. Moreover, the loading platens were modified with the purpose of inducing an eccentricity $e = h/4$ (h, the specimen height) in the compression load N. This testing condition leads to a linear variation of the stress σ orthogonal to the cross section of the specimen (and thus parallel to the grain):

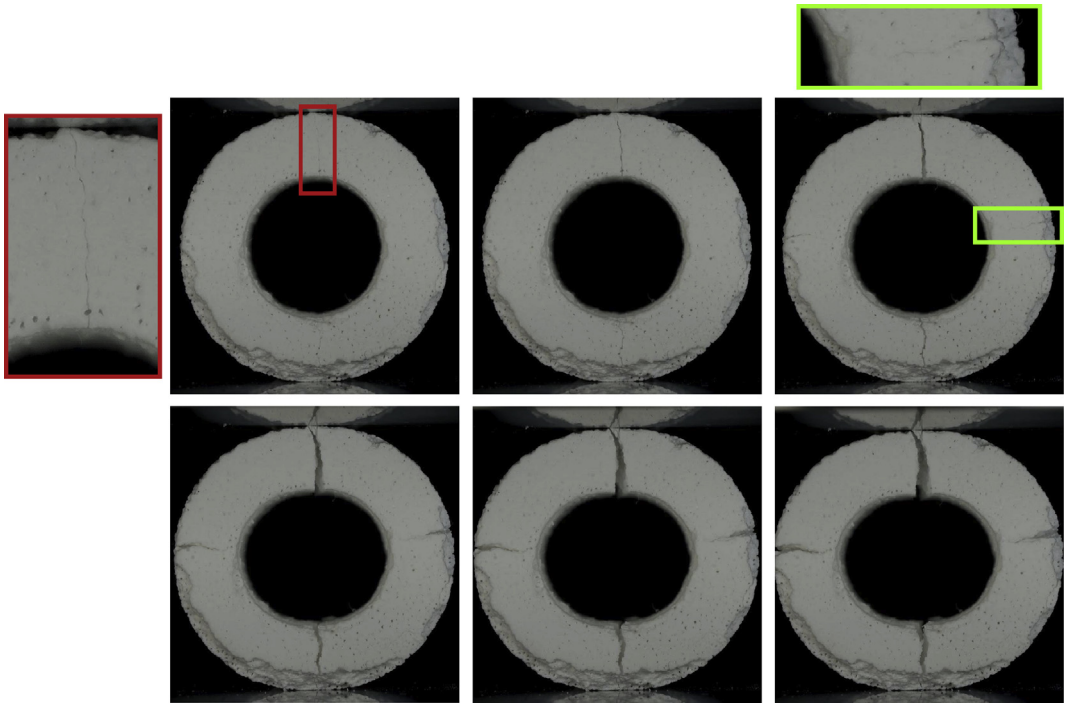

Fig. 16. A sequence of photos taken during a ring compression test on biomorphic apatite (BA) tubular samples (set #3) tested in the direction orthogonal to the grain. The growth of tensile fractures is clearly documented (see the insets).

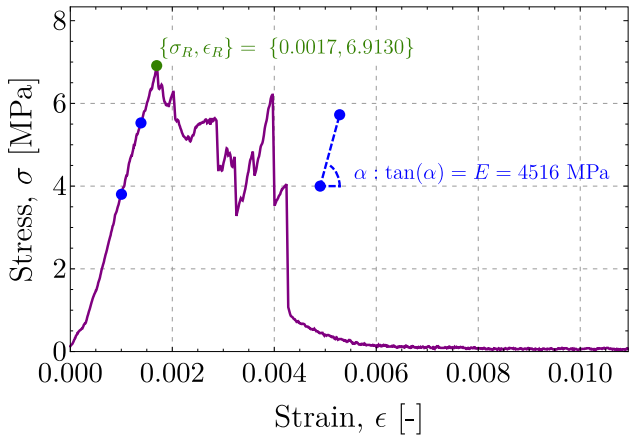

Fig. 17. Tensile stress/strain behavior of BA (Set #3) from a ring compression test, with tensile stress parallel to the grain. The green spot identifies the peak strength, and a straight line drawn through the two indicated blue spots was used to evaluate the Young modulus $E = \tan\alpha$. The high toughness of BA is highlighted by the slow load fall. BA, biomorphic apatite.

$$\sigma = \frac{N}{A} + \frac{Ne}{bh^3/12} y, \tag{6}$$

where A is the cross-sectional area of the specimen, b is its width, and y picks up the position along the cross section. At the extrados, $y = -h/2$, which corresponds to the upper side of the BA specimen observed in the SEM, the axial stress reaches its maximum positive value, corresponding to a tensile stress, whereas at the opposite side, compression prevails. This stress state leads to a very peculiar failure mode, where exfoliation of a thick layer of BA parallel to the grain takes place, followed by the final failure by transverse cracking on the side subjected to tension (see Fig. 22). The corresponding stress/strain curve represents the evolution of the tensile stress at the extrados, which is denoted with a black line in Fig. 19, labeled as 'eccentric compression.' The failure strength (parallel to the grain) approaches 6 MPa in tension, which is consistent with data reported in Table 9 obtained from three-point bending tests.

4. BA vs. wood and bone: the Ashby plot

The mechanical behavior of BA is now compared with that of its parent material, rattan wood, used to produce the BA, and with that of human bones. Tests have been conducted on rattan wood, obtained from a plant belonging to the subfamily of Calamoideae, mechanical properties of which have been investigated through compression and three-point bending experiments (performed following the standards

Table 7
Mechanical characteristics from ring tests on BA samples (tensile stresses are orthogonal to the grain).

Sample set	Geometrical properties				Ring test		
	H [mm]	r_o [mm]	r_i [mm]	ρ [g/cm^3]	$\sigma_{t,\perp}$ [MPa]	$E_{f,\perp}$ [MPa]	ρ/ρ_0 [−]
# 3	30.85	12.79	6.54	1.572	6.0 ± 0.94	2851 ± 1152	1.1

BA, biomorphic apatite.
All the samples are tubular, with the following average dimensions: H depth; r_o outer radius; r_i internal radius, and ρ density. On the right, the following average properties ($\pm$ standard deviation) are reported (from left to right): tensile strength and Young modulus. Finally, ρ/ρ_0 is the ratio between the density and the reference density of 1.47 g/cm^3 to which all mechanical values have been reported.

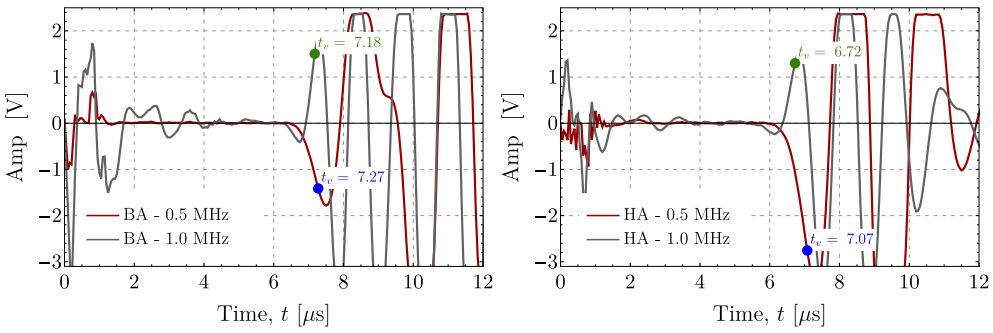

Fig. 18. Amplitude of the signal versus time for two ultrasonic tests on a BA sample (set #1, on the left) and on a HA sample (set #1, on the right) at two different frequencies (0.5 and 1.0 MHz). Note that the points that have been identified as the representative of the time of flight t_v have been identified in agreement with the standards [60] so that the arrival of the P-wave has been marked at the instance when the leading edge of the first peak was reached at 80%. (The evaluation of the time of flight was performed automatically using a Mathematica routine *ad hoc* developed.) BA, biomorphic apatite; HA, hydroxyapatite.

Table 8
Mechanical characteristics from ultrasonic tests on BA samples (parallel to the grain) and HA.

Set	Geometrical properties				Ultrasonic test			
	H [mm]	ϕ [mm]	A [mm^2]	ρ [g/cm^3]	v_p [m/s]	$\lambda + 2\mu$ [MPa]	E [MPa]	
							$\nu = 0$	$\nu = 0.25$
# 1,2	20.84	14.19	158.08	1.42	2723 ± 212	10398 ± 1661	10398 ± 1661	8665 ± 1384
HA 1,2	15.01	10.07	79.61	0.54	2191 ± 72	2583 ± 290	2583 ± 290	2152 ± 241

BA, biomorphic apatite; HA, hydroxyapatite.
All the samples are cylindrical, with the following average dimensions: H height; ϕ diameter; A cross-sectional area; and ρ density. On the right, the following average properties (± standard deviation) are reported (from left to right): wave velocity; uniaxial strain elastic modulus; and Young modulus for two different values of Poisson's ratio. All reported values have not been normalized to the reference density.

Table 9
Geometrical properties for the BA specimens tested in situ using a SEM and subjected to different loading conditions.

Loading condition	Geometrical properties				
	H [mm]	w [mm]	t [mm]	ρ/ρ_0 [−]	p (%)
Uniaxial compression (high friction)	31.47	20.52	10.11	0.91	57.29
Uniaxial compression (low friction)	31.29	21.29	10.53	0.93	56.21
Eccentric compression	31.55	21.46	10.22	0.95	55.83

SEM, scanning electron microscope; BA, biomorphic apatite.
H is the height of the sample, w is the width, and t is the thickness. ρ/ρ_0 is the ratio between the density and the reference density of 1.47 g/cm^3, and p is the porosity.

[61–64]), with the same configurations used for ceramics. A series of photos taken during a typical compression test are shown in Fig. 23, and the relative stress/strain curve is shown in Fig. 24 on the left, and the same figure presents a tensile stress/strain curve obtained from a three-point-bending test on the right.

Further results from the mechanical compression and three-point bending tests on rattan wood (with the stress always aligned parallel to the grain) are shown in Table 10, together with the geometrical properties of the samples.

Fig. 23 shows a failure process characterised by exfoliation by buckling, a long process highlighting the outstanding resistance of the material, while Fig. 24 shows a flat postelastic regime, characterized by large deformations. In rattan wood, failure may take different definitions so that it can be identified with the first load corresponding to visible local buckling of the fibers (I), with maximum curvature in the diagram (II), with the beginning of the plateau (III), with the peak (IV) in the curve, or, finally, (V) with the beginning of softening. Therefore, when

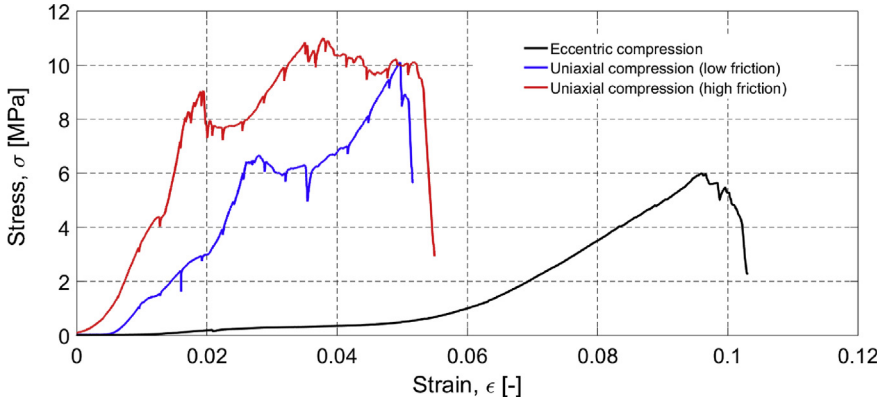

Fig. 19. Stress/strain curve of BA specimens tested in situ using a SEM under uniaxial compression at two levels of friction (at the specimen/platen contacts) and for eccentric loading. BA, biomorphic apatite; SEM, scanning electron microscope.

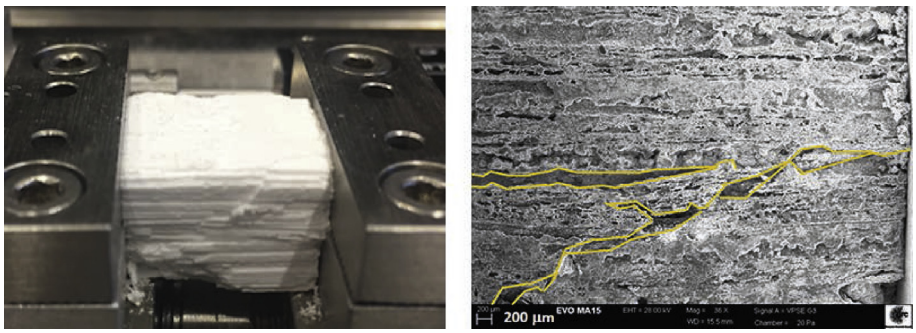

Fig. 20. Specimen tested under uniaxial compression with high friction. On the left: view of the specimen at failure; on the right: cracks at failure.

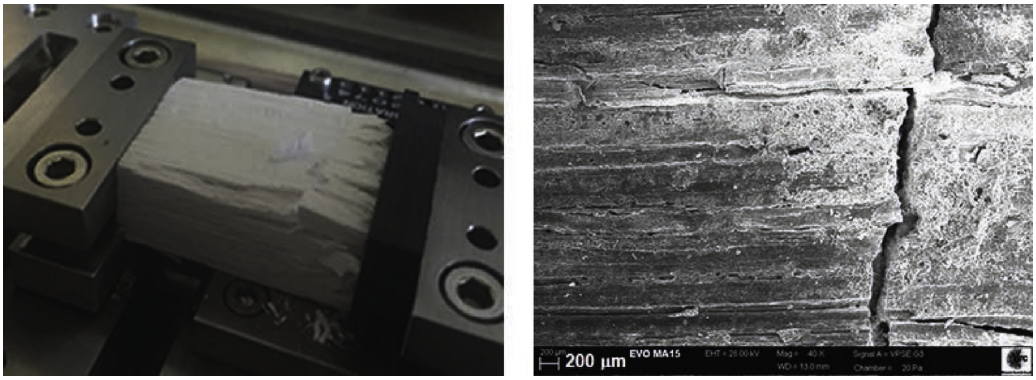

Fig. 21. Specimen tested under uniaxial compression by scanning electron microscopy under conditions of low friction. On the left: view of the specimen at failure (note the high-density polyethylene layer in black colour); on the right: cracks at failure.

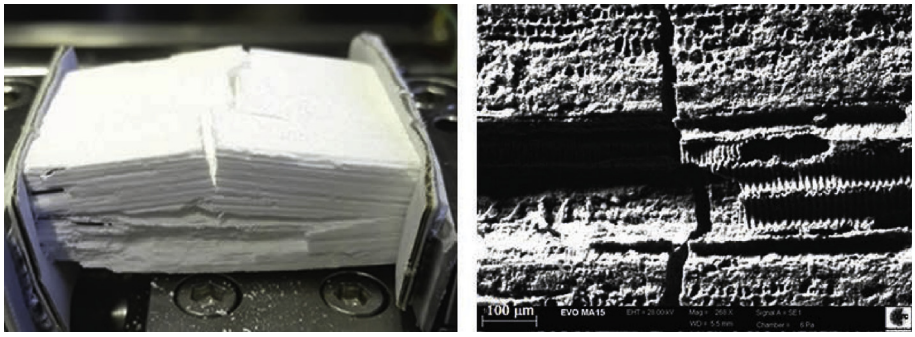

Fig. 22. BA specimen tested under eccentric compression in situ using a SEM and shown at failure on the left (note the paperboard layers in contact with the sample); cracks at failure are detailed on the right. BA, biomorphic apatite; SEM, scanning electron microscope.

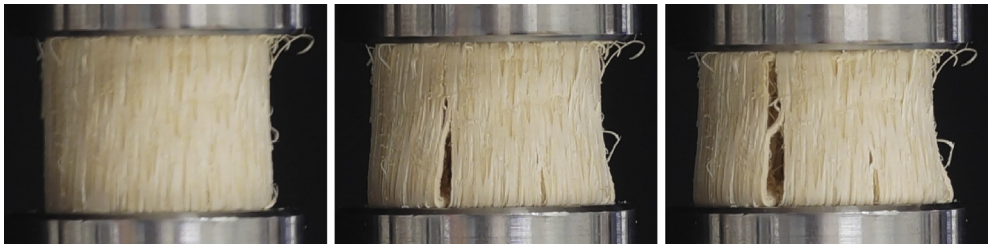

Fig. 23. A sequence of photos showing progressive failure (involving exfoliation by fiber buckling) of a rattan wood specimen during uniaxial compression.

failure is identified with the first appearance of local buckling of fibers, their strength in compression becomes lower than that in tension. It can be concluded that the behavior of rattan wood has several points in common with that of its derived material BA.

Bones are highly hierarchical composite materials so that their mechanical behavior is controlled by its two main constituents: cancellous bone (soft and deformable) and cortical bone (stiff and strong). Both of these materials are transversally isotropic [65–67], with stiffness and

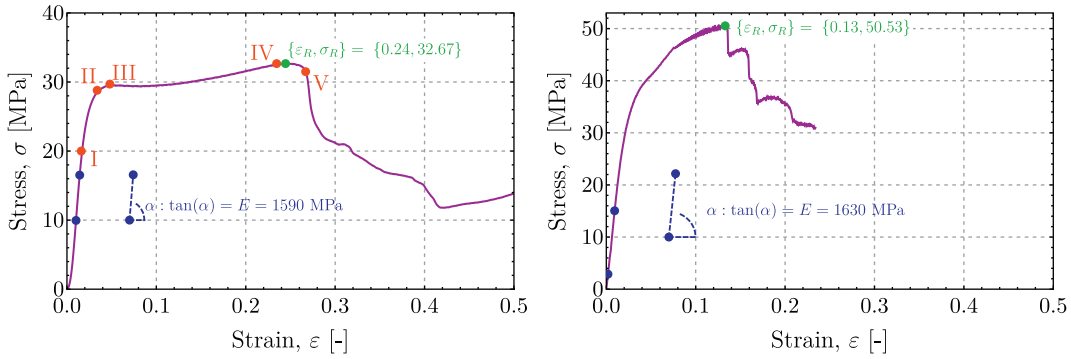

Fig. 24. Stress/strain behavior of a rattan wood sample subject to uniaxial compression (on the left) and three-point bending (on the right), parallel to the grain. The red spots (in the compression plot) identify different stress levels corresponding to different definitions of failure. A straight line drawn through the two indicated blue spots was used to evaluate the Young modulus $E = \tan\alpha$.

Table 10
Mechanical characteristics from uniaxial compression tests and three-point bending (in both cases, stress parallel to the grain) on rattan wood.

Tests	Geometrical properties			Mechanical parameters	
	H, L [mm]	ϕ [mm]	ρ [g/cm^3]	σ [MPa]	E [MPa]
Compression	29.18	21.90	0.46	23.7 ± 2.7	1326 ± 164
3-point bending	240	19.87	0.46	50.0 ± 11.8	2127 ± 415

All the samples are prismatic, with the following average dimensions: *H* height; *L* span; ϕ base dimension; and ρ density. On the right, the following average properties (± standard deviation) are reported (from left to right): compressive strength ad Young modulus.

strength different in tension and in compression [66–68] (see also the study by Cuppone et al [69]). Overall, the mechanical behavior of bone is also affected by the amount of cancellous vs. cortical bone so that for flat, long, and irregular bones, the mechanical properties are unique and different from one another [67,70–72].

The Ashby charts expressed in terms of Young modulus vs. strength and Young modulus vs. porosity for BA, loaded parallel (BA/ /) and perpendicular (BA⊥) to the grain, for the rattan wood used to produce the BA (parallel to the grain) and bones (data from the aforementioned literature) are shown in Fig. 1.

The Ashby charts show that BA is occupying a region usually not covered by ceramics; moreover, the Young modulus is fully compatible with values typical of wood and bone (particularly flat bone). If, on the one hand, the strength of BA is lower than that of bone and wood, on the other hand, it is much higher than that of the HA usually used for bone replacement. These considerations, in addition to the fact that porosity and the hierarchical structure of BA are similar to those of wood and bone, suggest that BA is a ceramic with outstanding mechanical characteristics, particularly suited for bone replacement and biological applications.

5. Conclusions

BA, a ceramic obtained through a biomorphic transformation process from rattan wood, presents a nanostructure and microstructure that retains elements inherited from its parent material, the ligneous essence. This structure has been shown to generate a lacunar fractal porosity, which yields the outstanding mechanical properties that we have measured for BA. In particular, BA shows a damage and defect tolerance, strength, and elastic stiffness superior to its competitor material, a porous sintered HA, but also to other biomorphic HAs obtained from different types of woods that are present in the literature [7,8,10]. Moreover, BA is transversely isotropic so that it can be effectively used in all the situations (for instance, bone replacement) where the ceramic piece is subjected to a load having a privileged direction. The fact that BA is produced without sintering and its superior mechanical performance suggest use of this material for several challenging biotechnologies.

Declaration of competing interest

The authors declare that they have no known competing financial interests or personal relationships that could have appeared to influence the work reported in this paper.

Acknowledgments

The authors are grateful to Mr. Flavio Vinante (University of Trento) for the invaluable help with the experiments. D.B. and R.C. acknowledge financial support from the PRIN 2015 'Multi-scale mechanical models for the design and optimization of micro-structured smart materials and metamaterials' 2015LYYXA8-006. D.M., M.P., A.R., S.S., and A.T. acknowledge financial support from ERC-2013-ADG-340561-INSTABILITIES.

References

[1] P. Fratzl, R. Weinkamer, Nature's hierarchical materials, Prog. Mater. Sci. 52 (2007) 1263–1334.
[2] R. Weinkamer, P. Fratzl, Mechanical adaptation of biological materials - the examples of bone and wood, Mater. Sci. Eng. C-Mater. Biol. Appl. 31 (2011) 1164–1173.
[3] A.H. Hueuer, D.J. Fink, V.J. Laraia, J.L. Arias, P.D. Calvert, K. Kendall, G.L. Messing, J. Blackwell, P.C. Rieke, D.H. Thompson, A.P. Wheeler, A. Veis, A.I. Caplan, Innovative materials processing strategies: a biomimetic approach, Science 255 (1992) 1098–1105.
[4] C.E. Bryne, D.C. Nagle, Cellulose derived composites - a new method for materials processing, Mater. Res. Innov. 1 (1997) 137–144.
[5] P. Greil, Biomorphous ceramics from lignocellulosics, J. Eur. Ceram. Soc. 21 (2001) 105–118.
[6] G.W. Kooistra, V.S. Deshpande, H.N.G. Wadley, Hierarchical corrugated core sandwich panel concepts, J. Appl. Mech. 74 (2) (2007) 259–268.
[7] C.R. Rambo, T. Andrade, T. Fey, H. Sieber, A.E. Martinelli, P. Greil, Microcellular Al_2O_3 Ceramics from wood for filter applications, J. Am. Ceram. Soc. 91 (3) (2008) 852–859.
[8] J. Qian, Y. Kang, W. Zhang, Z. Li, Fabrication, chemical composition change and phase evolution of biomorphic hydroxyapatite, J. Mater. Sci. Mater. Med. 19 (2008) 3373–3383.
[9] W.R. Legant, A. Pathak, M.T. Yang, V.S. Deshpande, R.M. McMeeking, C.S. Chen, Microfabricated tissue gauges to measure and manipulate forces from 3D microtissues, Proc. Natl. Acad. Sci. 106 (25) (2009) 10097–10102.
[10] C. Eichenseer, J. Will, M. Rampf, S. Wend, P. Greil, Biomorphous porous hydroxyapatite-ceramics from rattan (Calamus Rotang), J. Mater. Sci. Mater. Med. 21 (2010) 131–137.

[11] F.P.W. Melchels, K. Bertoldi, R. Gabbrielli, A.H. Velders, J. Feijen, D.W. Grijpma, Mathematically defined tissue engineering scaffold architectures prepared by stereolithography, Biomaterials 31 (2010) 6909–6916.
[12] N.A. Fleck, V.S. Deshpande, M.F. Ashby, Micro-architectured materials: past, present and future, Proc. R. Soc. A 466 (2010) 2495–2516.
[13] L. Bardella, A. Sfreddo, C. Ventura, M. Porfiri, N. Gupta, A critical evaluation of micromechanical models for syntactic foams, Mech. Mater. 50 (2012) 53–69.
[14] A. Vigliotti, D. Pasini, Mechanical properties of hierarchical lattices, Mech. Mater. 62 (2013) 32–43.
[15] F. Libonati, A.K. Nair, L. Vergani, M.J. Buehler, Mechanics of collagen–hydroxyapatite model nanocomposites, Mech. Res. Commun. 58 (2014) 17–23.
[16] C.T. Bauer, E. Kroner, N.A. Fleck, E. Arzt, Hierarchical macroscopic fibrillar adhesives: in situ study of buckling and adhesion mechanisms on wavy substrates, Bioinspiration Biomim. 10 (2015), 066002.
[17] A. Buehrig-Polaczek, C. Fleck, T. Speck, P. Schueler, S.F. Fischer, Biomimetic cellular metals-using hierarchical structuring for energy absorption, Bioinspiration Biomim. 11 (4) (2016).
[18] M. Fraldi, G. Perrella, M. Ciervo, F. Bosia, N.M. Pugno, A hybrid deterministic-probabilistic approach to model the mechanical response of helically arranged hierarchical strands, J. Mech. Phys. Solids 106 (2016) 338–352.
[19] F. Ongaro, E. Barbieri, N.M. Pugno, The in-plane elastic properties of hierarchical composite cellular materials: synergy of hierarchy, material heterogeneity and cell topologies at different levels, Mech. Mater. 103 (2016) 135–147.
[20] F. Ongaro, P. De Falco, E. Barbieri, N.M. Pugno, Mechanics of filled cellular materials, Mech. Mater. 97 (2016) 26–47.
[21] F. Libonati, G.X. Gu, Z. Qin, L. Vergani, M.J. Buehler, Bone–inspired materials by design: toughness amplification observed using 3D printing and testing, Adv. Eng. Mater. 18 (8) (2016), 1299-1299.
[22] G.X. Gu, F. Libonati, S.D. Wettermark, M.J. Buehler, Unraveling the role of nacre's mineral bridges, J. Mech. Behav. Biomed. Mater. 76 (2017) 135–144.
[23] Z.L. Yu, N. Yang, L.C. Zhou, et al., Bioinspired polymeric woods, Sci. Adv. 4 (2018) eaat7223.
[24] L. Zorzetto, D. Ruffoni, Wood-inspired 3D-printed helical composites with tunable and enhanced mechanical performance, Adv. Funct. Mater. 28 (2018) 1804510.
[25] F. Auricchio, A. Bacigalupo, L. Gambarotta, M. Lepidi, S. Morganti, F. Vadalàc, A novel layered topology of auxetic materials based on the tetrachiral honeycomb microstructure, Mater. Des. 179 (2019).
[26] U. Sabu, G. Logesh, M. Rashad, A. Joy, M. Balasubramanian, Microwave assisted synthesis of biomorphic hydroxyapatite, Ceram. Int. 45 (2019) 6718–6722.
[27] A. Tampieri, A. Ruffini, A. Ballardini, M. Montesi, S. Panseri, F. Salamanna, M. Fini, S. Sprio, Heterogeneous chemistry in the 3-D state: an original approach to generate bioactive, mechanically-competent bone scaffolds, Biomater. Sci. 7 (2019) 307–321.
[28] A. Tampieri, S. Sprio, A. Ruffini, Study of the hydrothermal transformation of wood-derived calcium carbonate into 3D hierarchically organized hydroxyapatite, Chem. Eng. J. 217 (2013) 150–158.
[29] A. Tampieri, S. Sprio, A. Ruffini, G. Celotti, I.G. Lesci, N. Roveri, From wood to bone: multi-step process to convert wood hierarchical structures into biomimetic hydroxyapatite scaffolds for bone tissue engineering, J. Mater. Chem. 19 (2009) 4973–4980.
[30] J. Szekely, Gas-solid Reactions, first ed., Academic Press, 1976, ISBN 9780323151399.
[31] R.I. Martin, P.W. Brown, Mechanical properties of hydroxyapatite formed at physiological temperature, J. Mater. Sci. Mater. Med. 6 (1995) 138–143.
[32] A.J. Wagoner Johnson, B.A. Herschler, A review of the mechanical behavior of CaP and CaP/polymer composites for applications in bone replacement and repair, Acta Biomater. 7 (2011) 16–30.
[33] J. Cao, C.R. Rambo, H. Sieber, Preparation of porous Al_2O_3-Ceramics by Biotemplating of wood, J. Por. Mat. 11 (2004) 163–172.
[34] C.R. Rambo, H. Sieber, Novel synthetic Route to biomorphic Al_2O_3 ceramics, Adv. Mater. 17 (8) (2005) 1088–1091.
[35] M. Singh, Bo-Moon Yee, Reactive processing of environmentally conscious, biomorphic ceramics from natural wood precursors, J. Eur. Ceram. Soc. 24 (2) (2004) 209–217.
[36] J. Cao, O. Rusina, H. Sieber, Processing of porous TiO_2-ceramics from biological preforms, Ceram. Int. 30 (7) (2004) 1971–1974.
[37] X. Li, T. Fan, Z. Liu, J. Ding, Q. Guo, D. Zhang, Synthesis and hierarchical pore structure of biomorphic manganese oxide derived from woods, J. Eur. Ceram. Soc. 26 (2006) 3657–3664.
[38] P. Greil, T. Lifka, A. Kaindl, Biomorphic cellular silicon carbide ceramics from wood: I. Processing and microstructure, J. Eur. Ceram. Soc. 18 (1998) 1961–1973.
[39] P. Greil, T. Lifka, A. Kaindl, Biomorphic cellular silicon carbide ceramics from wood: 2. Mechanical properties, J. Eur. Ceram. Soc. 18 (1998) 1975–1983.
[40] S. Binghe, F. Tongxiang, Z. Di, T. Okabe, The synthesis and microstructure of morph-genetic TiC/C ceramics, Carbon 42 (2004) 177–182.
[41] C.R. Rambo, J. Cao, O. Rusina, H. Sieber, Manufacturing of biomorphic (Si, Ti, Zr)-carbide ceramics by sol–gel processing, Carbon 43 (2005) 1174–1183.
[42] L. Esposito, D. Sciti, A. Piancastelli, A. Bellosi, Microstructure and properties of porous b-SiC template from soft woods, J. Eur. Ceram. Soc. 24 (2004) 533–540.
[43] V.E. Tarasov, Elasticity of fractal materials using the continuum model with non-integer dimensional space, Comptes Rendus Méchanique 343 (1) (2015) 57–73.
[44] V. Kunin, S. Yang, Y. Cho, P. Deymier, D.J. Srolovitz, Static and dynamic elastic properties of fractal-cut materials, Extreme Mech. Lett. 6 (2016) 103–114.
[45] X. Zhai, J. Gao, Y. Nie, N. Kedir, B. Claus, T. Sun, K. Fezzaa, X. Xiao, W.W. Chen, Real-time visualisation of dynamic fractures in porcine bones and the loading-rate effect on their fracture toughness, J. Mech. Phys. Solids 131 (2019) 58–371.
[46] D. Yin, B. Chen, W. Ye, J. Gou, J. Fan, Mechanical test and fractal analysis on anisotropic fracture of cortical bone, Appl. Surf. Sci. 357 (2015) 2063–2068.
[47] ASTM C1424 - 04 Standard Test Method for Monotonic Compressive Strength of Advanced Ceramics at Ambient Temperature.
[48] ASTM C1161 - 18 Standard Test Method for Flexural Strength of Advanced Ceramics at Ambient Temperature.
[49] F. Libonati, A.K. Nair, L. Vergani, M.J. Buehler, Fracture mechanics of hydroxyapatite single crystals under geometric confinement, J. Mech. Behav. Biomed. Mater. 20 (2013) 184–191.
[50] M. Gei, D. Bigoni, S. Guicciardi, Failure of silicon nitride under uniaxial compression at high temperature, Mech. Mater. 36 (2004) 335–345.
[51] M. Brun, L. Casnedi, G. Pia, Bending strength of porous ceramics tiles: bounds and estimates of effective properties of an Intermingled Fractal Units' model, Ceram. Int. 44 (9) (2018) 10241–10248.
[52] S. Timoshenko, J.N. Goodier, Theory of Elasticity, Ed. 2, McGraw-Hill, 1951.
[53] S. Timoshenko, On the distribution of stresses in a circular ring compressed by two forces acting along a diameter, London, Edinburgh, Dublin Philos. Mag. J. Sci. 44 (1922) 1014–1019.
[54] Ripperger, E.A., Davids, N., Critical stresses in a circular ring, Trans. Am. Soc. Civ. Eng., Paper No. 2308, pag. 619-629.
[55] J.C. Jeager, R. Hoskins, Stresses and failure in rings of rock load in diametral tension or compression, Br. J. Appl. Phys. 17 (1966) 685–695.
[56] D.W. Hobbs, The tensile strength of rocks, Int. J. Rock Mech. Min. Sci. 1 (1963) 385–396.
[57] J.A. Hudson, Tensile strength and the ring test, Int. J. Rock Mech. Min. Sci. 6 (1968) 91–97.
[58] Srinath, L.S., Acharya, Y.V.G., Stresses in a circular ring, Appl. Sci. Res., 1954, Sec. A Vol. 4, pag. 189-194.
[59] B.H. Choi, Y.K. Lee, C. Park, C.H. Ryu, C. Park, Measurement of tensile strength of brittle rocks using a half ring shaped specimen, Geosci. J. 23 (4) (2019) 649–660.
[60] UNI EN 583-3 - Non Destructive Testing - Ultrasonic Examination - Transmission Technique.
[61] BS EN 408-2010-A1, Timber Structures. Structural Timber and Glued Laminated Timber. Determination Of Some Physical and Mechanical Properties, 2012.
[62] ISO 8375, Timber Structures – Glued Laminated Timber – Test Methods for Determination of Physical and Mechanical Properties, 2009.
[63] ISO/TR 22157-1, Bamboo – Determination Of Physical and Mechanical Properties – Part 1: Laboratory Manual, 2004.
[64] ISO/TR 22157-2, Bamboo – Determination Of Physical and Mechanical Properties – Part 2: Requirements, 2004.
[65] A.A. Abdel-Wahab, K. Alam, V.V. Silberschmidt, Analysis of anisotropic viscoelastoplastic properties of cortical bone tissues, J. Mech. Behav. Biomed. Mater. 4 (5) (2011) 807–820.
[66] Y.C. Fung, Biomechanics: Mechanical Properties of Living Tissues, second ed., Springer, 1993.
[67] Y.H. An, R.A. Draughn, Mechanical Testing of Bone and the Bone-Implant Interface, CRC Press, 2000.
[68] S. Li, E. Demirci, V.V. Silberschmidt, Variability and anisotropy of mechanical behavior of cortical bone in tension and compression, J. Mech. Behav. Biomed. Mater. 21 (2013) 109–120.
[69] M. Cuppone, B.B. Seedhom, E. Berry, A.E. Ostell, The longitudinal young's modulus of cortical bone in the midshaft of human femur and its correlation with CT scanning data, Calcif. Tissue Int. 74 (2004) 302–309.
[70] K.V. Arun, K.K. Jadhav, Behaviour of human femur bone under bending and impact loads, Eur. J. Clin. and Biomed. Sci. 2 (2) (2016) 6–13.
[71] J.H. McElhaney, J.L. Fogle, J.W. Melvin, R.R. Haynes, V.L. Roberts, N.M. Alem, Mechanical properties of cranial bone, J. Biomech. 3 (1970) 495–511.
[72] M. Biggemann, D. Hilweg, P. Brinckmann, Prediction of the compressive strength of vertebral bodies of the lumbar spine by quantitative computed tomography, Skelet. Radiol. 17 (1988) 264–269.